SCIENCE CHINA Materials ARTICLES

mater.scichina.com link.springer.com

Published online 11 May 2018 | https://doi.org/10.1007/s40843-018-9274-y
Sci China Mater 2019, 62(1): 43–53

Unconventional solution-phase epitaxial growth of organic-inorganic hybrid perovskite nanocrystals on metal sulfide nanosheets

Zhipeng Zhang[1], Fangfang Sun[1], Zhaohua Zhu[1], Jie Dai[1], Kai Gao[1], Qi Wei[1], Xiaotong Shi[1], Qian Sun[1], Yan Yan[1], Hai Li[1], Haidong Yu[1], Guichuan Xing[1,2*], Xiao Huang[1*] and Wei Huang[1,3*]

ABSTRACT **Epitaxial heterostructures based on organic-inorganic hybrid perovskites and two-dimensional materials hold great promises in optoelectronics, but they have been prepared only *via* solid-state methods that restricted their practical applications. Herein, we report cubic-phased $MAPbBr_3$ ($MA=CH_3NH_3^+$) nanocrystals were epitaxially deposited on trigonal/hexagonal-phased MoS_2 nanosheets in solution by facilely tuning the solvation conditions. In spite of the mismatched lattice symmetry between the square $MAPbBr_3$ (001) overlayer and the hexagonal MoS_2 (001) substrate, two different aligning directions with lattice mismatch of as small as 1% were observed based on the domain-matching epitaxy. This was realized most likely due to the flexible nature and absence of surface dangling bonds of MoS_2 nanosheets. The formation of the epitaxial interface affords an effective energy transfer from $MAPbBr_3$ to MoS_2, and as a result, paper-based photodetectors facilely fabricated from these solution-dispersible heterostructures showed better performance compared to those based on MoS_2 or $MAPbBr_3$ alone. In addition to the improved energy transfer and light adsorption, the use of MoS_2 nanosheets provided flexible and continuous substrates to connect the otherwise discrete $MAPbBr_3$ nanocrystals and achieved the better film forming ability. Our work suggests that the scalable preparation of heterostructures based on organic-inorganic hybrid perovskites and 2D materials *via* solution-phase epitaxy may bring about more opportunities for expanding their optoelectronic applications.**

Keywords: organic-inorganic hybrid perovskite, transition metal chalcogenide, epitaxial growth, paper-based photodetector

INTRODUCTION

In the past decade, intensive research effort has been devoted to two-dimensional (2D) layered materials [1–3]. Among the various 2D materials, transition metal dichalcogenide (TMDs) nanosheets have drawn particular attention due to their promises in electrocatalysis [4], electronics [5], optoelectronics [6] and so on. However, in terms of light-conversion/emitting properties, semiconducting TMDs generally exhibited low quantum efficiencies partly due to their large specific surface area accompanied with a high density of surface defects that can act as recombination centers [7]. Besides, TMD nanosheets exhibited limited light-absorbing ability because of their atomic-scale thicknesses. For instance, a single-layer MoS_2 absorbed only 10 % of incident photons at its excitonic resonances (i.e., 615 and 660 nm) [8]. Much effort has thus been made to create TMD-based heterostructures like MoS_2/graphene [9] and MoS_2/WS_2, [10] to improve the efficiency of charge separation/transport. Enhanced light absorption has also been achieved by hybridizing TMDs with noble metal nanoparticles [11], organic dyes [12], silicon (Si) [13], carbon nanotubes [14] and so on.

Organic-inorganic hybrid perovskites (e.g., $CH_3NH_3PbI_3$) have recently emerged as a class of promising optoelectronic materials [15–17]. Solar cells based on them have achieved remarkable power conversion efficiencies exceeding 20% [18–20]. The excellent performance has been attributed to a combination of several attractive features such as a high and balanced carrier mobility [21], long carrier diffusion length [22] and large light absorp-

[1] Key Laboratory of Flexible Electronics (KLOFE) & Institute of Advanced Materials (IAM), Jiangsu National Synergistic Innovation Center for Advanced Materials (SICAM), Nanjing Tech University (NanjingTech), Nanjing 211816, China
[2] Institute of Applied Physics and Materials Engineering, University of Macau, Macau SAR 999078, China
[3] Shaanxi Institute of Flexible Electronics (SIFE), Northwestern Polytechnical University (NPU), Xi'an 710072, China
* Corresponding authors (emails: iamgcxing@njtech.edu.cn (Xing G); iamxhuang@njtech.edu.cn (Huang X); iamwhuang@njtech.edu.cn (Huang W))

tion coefficient in the UV–vis range [23]. Recently, organic-inorganic hybrid perovskites in the form of colloidal nanocrystals (NCs) have been reported [24,25], and compared to their bulk counterpart, they present a number of advantages such as a high photoluminescence (PL) quantum yield [26], narrow-band emission [27] and shape-dependent PL [28]. These merits make them especially attractive for applications such as solution-processed photodetectors [29], light-emitting diodes [30] and solar cells [31]. Unfortunately, colloidal NCs with small lateral sizes suffer from poor film-forming ability, restricting their use in applications where continuous films for charge transporting are required. Recently, TMDs and organic-inorganic hybrid perovskites have been combined into heterostructures, with the aim to marrying their good electronic and optical properties [32–37]. For example, photoconductors based on WSe_2/$CH_3NH_3PbI_3$ [34] and WS_2/$CH_3NH_3PbI_3$ [35] demonstrated superior photo-responsive performance compared to single-component devices. However, such heterojunctions have been realized mostly *via* solid-state methods typically involving chemical vapor deposition (CVD), [35] mechanical exfoliation [36] and/or dry transfer [33], which are difficult to scale-up for practical applications. Direct growth of perovskite crystals on dispersible 2D materials in solution is expected to enable the scalable production of solution-processible heterostructures, but has not been realized, because a non-polar solvent is usually needed for the precipitation of perovskite crystals [38,39] which is incompatible with most solvation conditions for 2D materials.

In this contribution, we demonstrated a facile wet-chemical method to directly grow organic-inorganic hybrid perovskite ($MAPbBr_3$, MA=$CH_3NH_3^+$) NCs on surfaces of dispersible MoS_2 nanosheets. Two unusual symmetry-mismatched epitaxial relationships were observed, thanks to the use of flexible and dangling-bond-free MoS_2 nanosheets. We further applied the $MAPbBr_3$/MoS_2 epitaxial heterostructures in paper-based photodetector with the much improved performance compared to their single components.

EXPERIMENTAL SECTION

Materials: $PbBr_2$ (lead (II) bromide, 99.999%, Sigma-Aldrich, Germany), CH_3NH_3Br (methylammonium bromide, ≥99.5%, Xi'an Polymer Light Technology Co., Ltd., China), oleic acid (OA, >85.0%, TCI, Japan), *n*-octylamine (OLA, >98.0%, TCI, Japan), molybdenum disulfide (MoS_2, <2 μm, 99%, Sigma-Aldrich, Germany), acetylene black (Li Zhiyuan Co., Ltd., China), poly(vinylidene fluoride) (PVDF, Shanghai Chemical Reagent Co., Ltd., China), *N*,*N*-dimethylformamide (DMF, analytical reagent, Shanghai Chemical Reagent Co., Ltd., China), toluene (analytical reagent, Shanghai Chemical Reagent Co., Ltd., China), acetone (analytical reagent, Shanghai Chemical Reagent Co., Ltd., China) and *N*-methyl-2-pyrrolidone (NMP, analytical reagent, Shanghai Chemical Reagent Co., Ltd., China) were used as received without further purification. The deionized (DI) water was purified using Milli-Q3 System (Millipore, France).

Preparation of MoS_2 nanosheets: MoS_2 nanosheets were prepared by a previously reported electrochemical lithium intercalation and exfoliation method [40]. Layered bulk MoS_2 crystals were mixed with acetylene black and PVDF binder dispersed in NMP. This mixture was then uniformly coated on a copper foil and dried under vacuum overnight. The intercalation was conducted in a battery test cell using a Li foil as the anode, and the MoS_2 crystals coated on copper foil as the cathode. Assembly of the test cells was conducted in an Ar-filled glove box. The electrochemical Li intercalation was accomplished in a Land battery test system at a constant current density of 0.025 mA. After the discharge process, the Li-intercalated MoS_2 was washed with acetone, followed by exfoliation under ultrasonication in DI water in a closed vial to give a suspension of isolated nanosheets. The product was centrifuged at 3,000 rpm for 20 min to remove the precipitate containing thicker crystals and the supernatant was washed three times with DMF before further use.

Preparation of $MAPbBr_3$/MoS_2 heterostructure: 0.1 mL of the aforementioned MoS_2 suspension in DMF (~1 mg mL^{-1}) was added dropwise into 3 mL toluene under ultrasonication to form a homogeneous suspension denoted as solution A. Then 0.16 mmol CH_3NH_3Br and 0.2 mmol $PbBr_2$ was dissolved in 5 mL of DMF together with 20 μL of OLA and 0.5 mL of OA to form a precursor solution B. After that, 20 μL of solution B was added dropwise into solution A with mild shake for 10 s. Upon mixing, a brownish green solution was formed. After centrifugation at 12,000 rpm for 10 min, the precipitates were collected and washed three times with toluene before further characterizations.

Fabrication of paper-based photodetector: a piece of commonly used writing paper (Deli, China) was used as the substrate. Two graphite electrodes with a 0.5 mm spacing were then drawn onto the paper using a 12B pencil (Fig. S7). After that, 3 μL of a concentrated dispersion of the $MAPbBr_3$/MoS_2 heterostructures (~5.0 mg mL^{-1}) was drop-casted between the electrodes.

Photoresponse measurements: the current–voltage

(I–V) and the current-time (I–t) curves of the photodetectors were measured on a 4200 semiconductor characterization system (Keithley, USA) in air at room temperature. A 405 nm laser was used for all the measurements. The actual power intensity was measured by a LP1 power meter (Sanwa Electric Instrument Co., Ltd., Japan). The responsivity (R) was calculated as $R = \Delta I/(P{\cdot}S)$, where ΔI is the difference between the photocurrent and the dark current, P is the incident power density, and S is the effectively illuminated area.

Characterizations: the morphological and structural characterizations of the products were conducted by transmission electron microscope (TEM, HT7700, Hitachi, Japan), high resolution transmission electron microscope (HRTEM, JEOL 2100F, Japan) and X-ray diffraction (XRD, SmartLab Rigaku, Japan, with Cu K_α radiation at λ = 1.54 Å). For the X-ray photoelectron spectroscopy (XPS, PHI 5000 VersaProbe, Japan) measurements, the binding energies were corrected for specimen charging effects using the C 1s level at 284.6 eV as the reference. UV-vis absorption spectra of the materials were measured on a UV-vis spectrophotometer (UV-1750, Shimadzu, Japan). PL spectra were taken using a F4600 fluorescence spectrometer (Hitachi, Japan). The time-resolved photoluminescence (TRPL) spectroscopy spectra were acquired using a FLSP920 fluorescence spectrophotometer (Edinburgh Instruments, England).

RESULTS AND DISCUSSION

Typically, MoS_2 nanosheets were prepared by electrochemical lithium intercalation and exfoliation based on a previous report (see the experimental section for the detailed procedure) [40]. Based on TEM and atomic force microscopy (AFM) measurements (Fig. S1), the as-prepared MoS_2 nanosheets were 200–500 nm in lateral size and 1.3–3.0 nm in thickness, suggesting that they are single- to few-layer thick [41]. The subsequent preparation of $MAPbBr_3/MoS_2$ heterostructures is schematically illustrated in Fig. 1a. First, the as-exfoliated MoS_2 nanosheets were redispersed in a mixed solvent composing of DMF and toluene with a volumetric ratio of V_{DMF}:$V_{toluene}$=1:30. To this MoS_2 suspension, a mixture of CH_3NH_3Br, $PbBr_2$, OA, and OLA in DMF was added dropwise with mild shake. Upon mixing, the solution color changed from brown to brownish green, indicating the formation of perovskite NCs. The scanning transmission electron microscopy (STEM) image in Fig. 1b clearly shows the deposition of $MAPbBr_3$ NCs with an average edge length of ~16.8 nm (Fig. S2) on the surface of a MoS_2 nanosheet. Fig. 1c, d are photographs of the obtained $MAPbBr_3/MoS_2$ solution under room light and UV irradiation (365 nm), respectively, indicating the good dispersibility and photoluminescent property of the heterostructures. Note that the average size of $MAPbBr_3$ NCs synthesized directly in solution without presence of MoS_2 was ~17.3 nm (Fig. S3) with a broader size distribution compared to those grown on MoS_2 (Fig. S2). This suggests that MoS_2 nanosheets as synthetic templates helped to control the nucleation process of $MAPbBr_3$ to give a relatively narrow size distribution.

It is important to note that in our synthesis, the use of a mixed solvent to disperse MoS_2 nanosheets is critical to realize the *in-situ* deposition of perovskite NCs on MoS_2. Based on previous reports, colloidal organic-inorganic hybrid perovskite NCs are usually prepared through ligand-assisted reprecipitation (LARP) methods [38,39], which began with the dissolution of lead halide and alkylammonium halide in a polar solvent like DMF together with surfactants such as OA and OLA. This precursor solution was then injected into a nonpolar solvent (e.g., toluene or hexane) under stirring, during which perovskite NCs were precipitated due to the decrease of solubility. To *in-situ* deposit perovskite NCs on 2D materials like MoS_2 nanosheets, the nanosheets as synthetic templates need to be dispersed in the nonpolar solvent. However, due to surface charges [42], as-exfoliated MoS_2 nanosheets cannot be dispersed in a nonpolar solvent. As evidently shown in Fig. 1e, while MoS_2 nanosheets were well-dispersed in DMF, they aggregated in toluene. Interestingly, when a small amount of DMF was added to toluene, for example, with a V_{DMF}:$V_{toluene}$ volume ratio of 1:30, the MoS_2 nanosheets were dispersed again after sonication, and the maximum concentration could reach ~0.9 mg mL^{-1} (Fig. S4). To find the optimal solvent condition for our synthesis, the critical DMF concentrations (as in toluene) at which MoS_2 nanosheets began to aggregate or $MAPbBr_3$ began to precipitate were determined, respectively (Fig. 1f). For a given $MoS_2/PbBr_2$ ratio (i.e., 1 mg MoS_2/0.8 mmol $PbBr_2$), the blue-shaded and red-shaded areas, which correspond to MoS_2 aggregation and $MAPbBr_3$ dissolution, respectively, should be avoided. The optimized condition used in the present study was presented as spot A in Fig. 1f, corresponding to a DMF concentration of 3.2 *v*% in toluene. In such case, the presence of a small amount of DMF ensured the good dispersion of MoS_2 nanosheets, and meanwhile maintained a low solvent polarity for the precipitation of perovskite NCs.

The XRD pattern of the heterostructures in Fig. 1g shows the characteristic peaks for cubic-phased ($Pm\bar{3}m$)

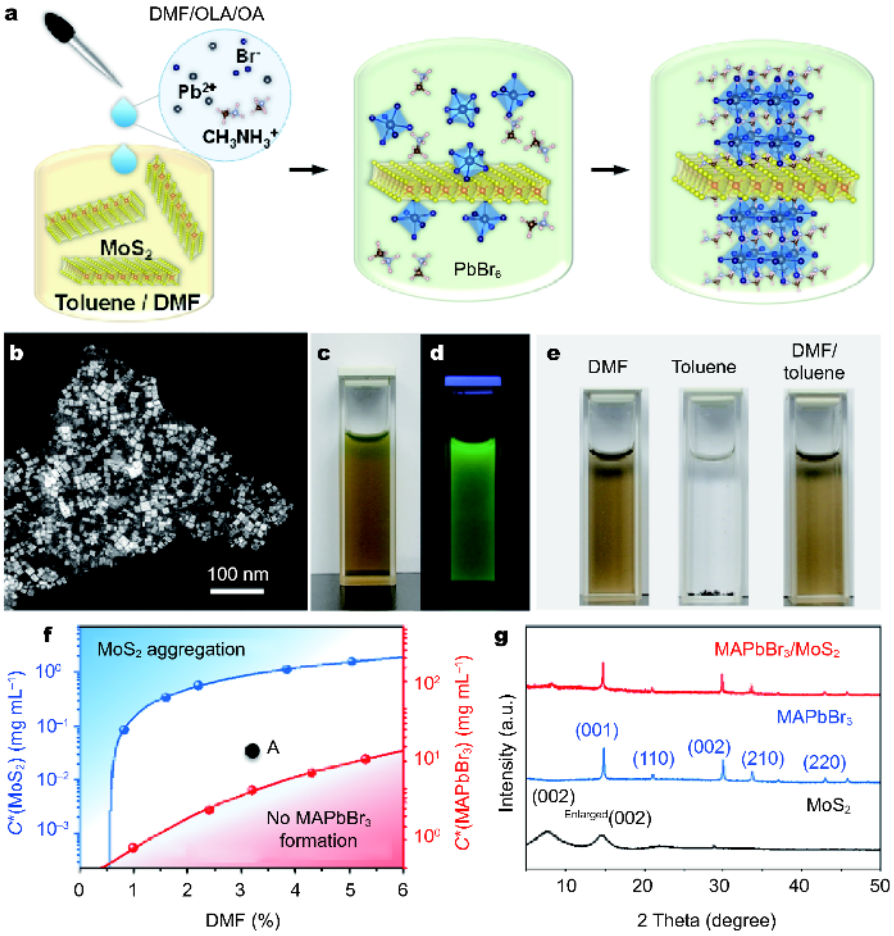

Figure 1 (a) Schematic illustration of the formation process of $MAPbBr_3/MoS_2$ heterostructures. (b) STEM image of a typical $MAPbBr_3/MoS_2$ heterostructure. Photographs of a solution containing as-synthesized $MAPbBr_3/MoS_2$ heterostructures (c) under room light and (d) under excitation of a 365 nm laser. (e) Photographs of MoS_2 nanosheets in toluene, DMF and toluene/DMF, respectively. (f) Plots of critical concentrations at which (blue) MoS_2 nanosheets began to aggregate and (red) $MAPbBr_3$ began to precipitate in a mixed DMF/toluene solution at different DMF concentrations (0–6 *v*%). (g) XRD patterns of as-prepared $MAPbBr_3/MoS_2$ heterostructures, $MAPbBr_3$ NCs and MoS_2 nanosheets.

$MAPbBr_3$ with a = 5.96 Å [43,44]. The peak at around 8° can be attributed to the enlarged lattice spacing of the MoS_2 (002) planes caused by lithium-intercalation (Fig. S5). The presence of the XRD peaks for both $MAPbBr_3$ and MoS_2 indicates the successful preparation of $MAPbBr_3/MoS_2$ heterostructures. Based on previous reports, MoS_2 nanosheets prepared by lithium intercalation and exfoliation are usually composed of both the hexagonal 2H and trigonal 1T polymorphs [45]. This was confirmed with XPS analysis (Fig. S6), based on which the concentration of the 1T phase was estimated to be ~84 %, indicating a highly metallic nature of the nanosheets [46,47]. HRTEM was then used to further study the microstructure of the heterostructures. As shown in Fig. 2a, an overlapping of lattice patterns of $MAPbBr_3$ and MoS_2 was observed, and the corresponding fast Fourier transformation (FFT)-generated diffraction pattern shows two sets of spots with a square symmetry (i.e., the vertices of the yellow square) and a hexgaonal symmetry (i.e., the vertices of the blue hexagon), respectively (Fig. 2b). By selecting the respective set of spots, the MoS_2 [001]-zone lattice pattern and the $MAPbBr_3$ [001]-zone pattern were re-generated and shown in Fig. 2c and d, respectively. Along the $MAPbBr_3$ [010]/MoS_2 [120] direction, the $MAPbBr_3$ (020) planes are parallel with the MoS_2 (010) planes with a 7% mismatch. Along the other direction, i.e., the $MAPbBr_3$ [100]/MoS_2 [100] direction, the mismatch between $MAPbBr_3$ (200) and MoS_2 ($2\bar{1}0$) planes is as large as 47%. To justify the epitaxial alignment in this direction, the domain-matching epitaxy was applied [48],

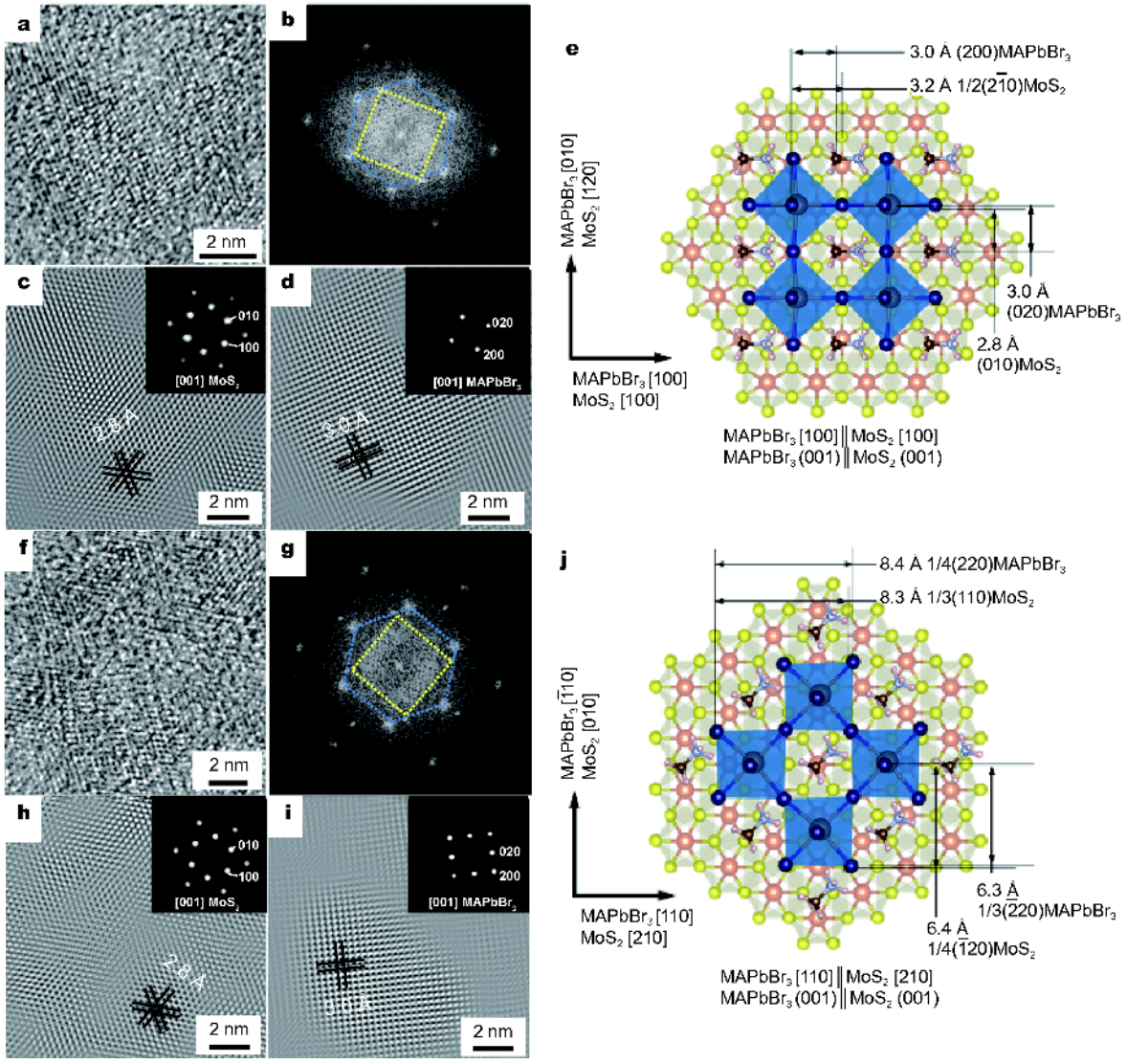

Figure 2 (a) HRTEM image of an area with overlapped lattices of $MAPbBr_3$ and MoS_2, and (b) the corresponding FFT-diffraction pattern. (c) MoS_2 [001]-zone and (d) $MAPbBr_3$ [001]-zone lattice patterns generated by performing inverse-FFT of the spots forming the blue hexagon and the yellow square in (b), respectively. Insets: the respectively selected spots. (e) Schematic model indicating the $MAPbBr_3$ [100]||MoS_2 [100] and $MAPbBr_3$ (001)||MoS_2 (001) epitaxial relationship. (f) HRTEM image of another area with overlapped lattices of $MAPbBr_3$ and MoS_2, and (g) the corresponding FFT-diffraction pattern. (h) MoS_2 [001]-zone and (i) $MAPbBr_3$ [001]-zone lattice patterns generated by performing inverse-FFT of the spots forming the blue hexagon and the yellow square in (g), respectively. Insets: the respectively selected spots. (j) Schematic model indicating the $MAPbBr_3$ [110]||MoS_2 [210] and $MAPbBr_3$ (001)||MoS_2 (001) epitaxial relationship.

in which the lattices of the two materials match through a domain that contains integral numbers of parallel atomic layers (Fig. S7). In our case, if we consider two times of the interlayer spacing of MoS_2 (2$\bar{1}$0) planes (i.e., the spacing for MoS_2 1/2(2$\bar{1}$0) planes), the mismatch between it and $MAPbBr_3$ (200) becomes only 6%, as shown in the epitaxial model in Fig. 2e. Because of the different lattice symmetry between the $MAPbBr_3$ (001) overlyer and MoS_2 (001) substrate, another possible surface alignment of $MAPbBr_3$ on MoS_2 was also observed (Fig. 2f–j). The HRTEM image of another area of overlapped lattice patterns is shown in Fig. 2f and its FFT-generated diffraction pattern is shown in Fig. 2g, based on which lattice patterns of the $MAPbBr_3$ [001]-zone axis and MoS_2 [001]-zone axis were re-generated and shown in Fig. 2h, i, respectively. It can be seen that $MAPbBr_3$ (220) and MoS_2

(100) planes are epitaxially aligned, but with a mismatch of as large as 24%. Therefore, domain-matching epitaxy is applied again. As shown in the schematic epitaxial model in Fig. 2j, the mismatch between $MAPbBr_3$ 1/4(220) and MoS_2 1/3(100) planes along the $MAPbBr_3$ [110]/MoS_2 [210] direction, and that between $MAPbBr_3$ 1/3($\bar{2}$20) and MoS_2 1/4($\bar{1}$20) planes along the $MAPbBr_3$ [$\bar{1}$10]/MoS_2 [010] direction are both ~1%. This suggests that the epitaxial growth of $MAPbBr_3$ on MoS_2 might be structurally favored. Up to now, epitaxial heterostructures of perovskites/2D materials have only been reported recently by the physical vapor deposition (PVD) of PbI_2 on a 2D material (e.g., BN or MoS_2) followed by reacting PbI_2 with CH_3NH_3I *via* CVD [32]. In that case, both PbI_2 and the 2D material exhibited the six-fold symmetry at the heterointerface. It has been known that to realize epitaxial heterostructures, a small misfit in both lattice symmetry and lattice parameters is usually required to achieve a minimum interfacial energy. Some exceptions have also been reported especially in recent cases of using van der Waals layered materials as substrates which are free from surface dangling bonds to effectively tolerate strains arising from a large symmetry/lattice mismatch [49–53]. Examples include recent demonstrations of epitaxial overgrowth of Pt(101) on MoS_2(001) [49] and PbSe(001) on Bi_2Se_3(001) [50]. Similarly, in our present work, the epitaxial deposition of $MAPbBr_3$ on MoS_2 with four-fold and six-fold symmetry at the interface, repectively, was realized in solution. This can be due to the dangling-bond-free surfaces of MoS_2 nanosheets, and their soft/flexible nature when dispersed in solution to tolerate the large symmetry mismatch [50]. For comparison, we carried out a control experiment by directly mixing pre-synthesized $MAPbBr_3$ NCs and MoS_2 nanosheets. $MAPbBr_3$ NCs were mostly separated from the MoS_2 nanosheets without contact, and epitaxial relationship was not observed (Fig. S8).

UV-vis absorption and PL spectra of the $MAPbBr_3$/MoS_2 heterostructure in comparison with those of $MAPbBr_3$ NCs and MoS_2 nanosheets without hybridization are shown in Fig. 3. The $MAPbBr_3$ NCs show an absorption peak at ~525 nm, corresponding to its direct band gap of 2.3 eV [28]. Compared to $MAPbBr_3$ or MoS_2, the heterostructure exhibited increased absorption in the UV-vis region. As for the PL property, the emission of $MAPbBr_3$ NCs at ~530 nm was dramatically quenched (by more than 90%) when they were *in-situ* deposited on MoS_2 nanosheets, based on the equal Pb^{2+} concentration (Fig. 3b). The MoS_2 nanosheets exhibited no visible PL

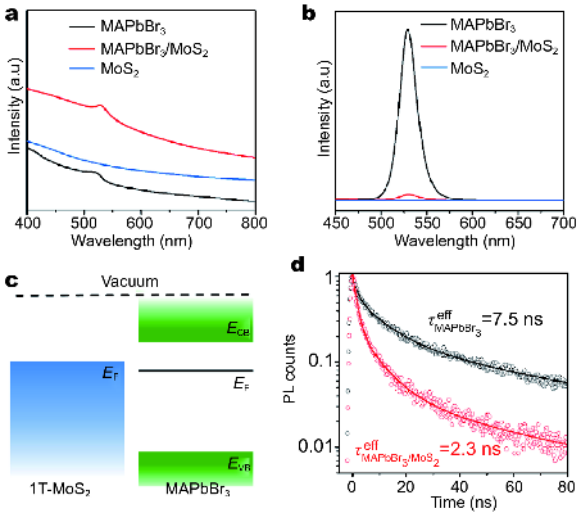

Figure 3 (a) UV-vis absorption and (b) PL spectra of the MAPbBr NCs, MoS_2 nanosheets and $MAPbBr_3$/MoS_2 heterostructures. (c) Schematic illustration of the energy band alignment at the $MAPbBr_3$/MoS_2 heterointerface. (d) TRPL spectra for $MAPbBr_3$ NCs and $MAPbBr_3$/MoS_2 heterostructures.

emission due to a high concentration of metallic 1T phase. The largely reduced PL intensity of $MAPbBr_3$ after hybridization with MoS_2 (Fig. 3b) suggests the effective energy transfer between them. This was also observed previously in perovskite/MoS_2 heterojunctions prepared by layer-by-layer assembly [36,37]. Indeed, the Fermi level of 1T MoS_2 (~3.9 eV) [45] was located below the conductive band of $MAPbBr_3$ (~3.6 eV) [54] as schematically shown in Fig. 3c, which might enable the effective transport of charge carriers and excitons from $MAPbBr_3$ to MoS_2. The efficient energy transfer between them was further verified by TRPL. As shown in Fig. 3d, TRPL spectra were collected at the emission center of $MAPbBr_3$ (i.e., 530 nm). The effective decay lifetime of the pure $MAPbBr_3$ ($\tau^{eff}_{MAPbBr_3}$) was measured as 7.5 ns while that for $MAPbBr_3$/MoS_2 ($\tau^{eff}_{MAPbBr_3/MoS_2}$) was 2.3 ns. This difference is likely caused by the energy transfer from $MAPbBr_3$ to MoS_2, and the transfer time, τ_{ET}, as estimated based on the equation below [21] is 3.3 ns, which is in the ns time scale of radiative recombination that ensures efficient PL quenching [21,55].

$$\frac{1}{\tau^{eff}_{MAPbBr_3/MoS_2}} = \frac{1}{\tau^{eff}_{MAPbBr_3}} + \frac{1}{\tau_{ET}}$$

The solution-processible $MAPbBr_3$/MoS_2 heterostructures prepared from the facile and scalable approach are suitable for fabrication of thin-film devices. As a proof-of-concept demonstration, paper-based photo-

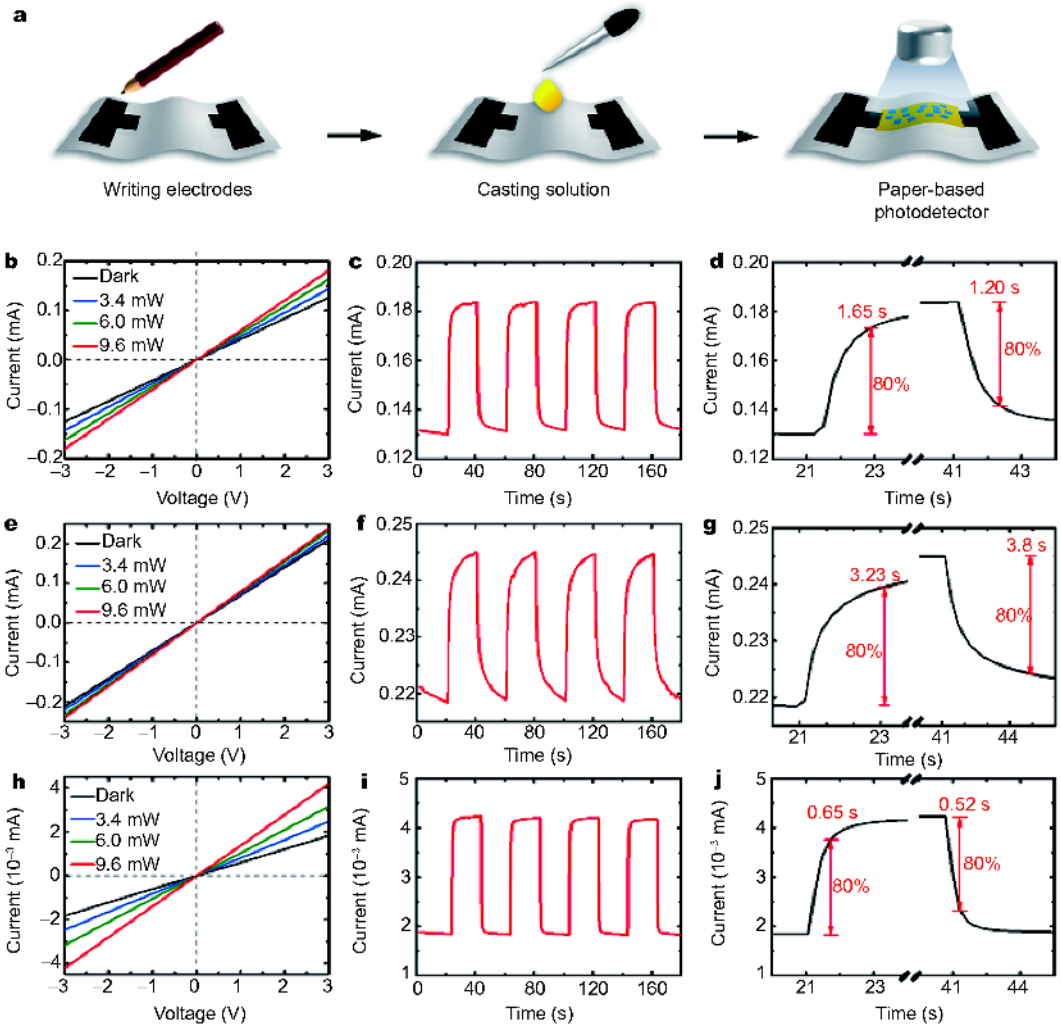

Figure 4 (a) Schematic illustration of the fabrication process of a paper-based photodetector. (b) *I*–*V* curves at different light intensity, (c) temporal photocurrent response and (d) a zoom-in view of the temporal photocurrent response of the photodetector based on $MAPbBr_3/MoS_2$ heterostructures. (e) *I*–*V* curves, (f) temporal photocurrent response and (g) a zoom-in view of the temporal photocurrent response of the photodetector based on MoS_2 nanosheets. (h) *I*–*V* curves, (i) temporal photocurrent response and (j) a zoom-in view of the temporal photocurrent response of the photodetector based on $MAPbBr_3/MoS_2$ heterostructures after they were partially transformed from 1T to 2H phase by irradiation with a 780 nm laser. The light source used for all measurements was a 405 nm laser.

detectors were fabricated based on the $MAPbBr_3/MoS_2$ heterostructures. Compared to the conventional silicon substrate and plastic substrates such as polyethylene terephthalate (PET) and polydimethylsiloxane (PDMS), paper is cheap and renewable and has been explored as a supplement to silicon and plastics in many areas [56,57]. More importantly, pencil traces (graphite) could be easily drawn on paper as electrodes, and the whole fabrication process takes ~10 min, much faster than making devices on plastics or silicon which normally requires thermally evaporated metal electrodes through a shadow mask [34,35]. As schematically shown in Fig. 4a, two graphite electrodes were firstly drawn on a piece of paper by using a 12B pencil (Fig. S9). After that, a solution of the heterostructures was drop-casted between the electrodes and then dried naturally before measurements. The $MAPbBr_3/MoS_2$ heterostructures deposited on paper formed a continuous film without obvious cracks (Fig. S10a–c). The linear and symmetrical current–voltage (*I*–*V*) curve of the device suggests that the $MAPbBr_3/MoS_2$ heterostructures formed a low resistance contact with the pencil trace electrodes (Fig. S10d) [58]. Fig. 4b

shows the *I*–*V* curves of the $MAPbBr_3/MoS_2$ paper-based photodetector under 405 nm laser illumination at varied power from 3.4 to 9.6 mW. A clear rise of the photocurrent with increasing illumination intensity was observed, indicating the effective conversion of photon flux to photogenerated carriers. However, the observed low on/off ratio, with a value of 1.41 at 9.6 mW, was due to the relatively large dark current which was caused by the high concentration of metallic 1T phase in the MoS_2 nanosheets [37]. The temporal photoresponse of the photodetector was measured under the periodic illumination of a 405 nm laser with an on/off interval of 20 s at a bias of 3 V. The $MAPbBr_3/MoS_2$ paper-based photodetector showed good on-off switching as shown in Fig. 4c. The rise time and decay time, as also important parameters for evaluating a photodetector, were measured as the time required for the photoresponse to increase by 80% from the minimum current and drop by 80% from the maximum current, respectively [37]. As shown in Fig. 4d, the rise and fall time of the $MAPbBr_3/MoS_2$ hybrid device was 1.65 and 1.20 s, respectively. Compared to the MoS_2-based device (Fig. 4e–g), the device based on $MAPbBr_3/MoS_2$ showed the improved on/off ratio, photoresponsivity and response rate (Fig. 4b–g and Table S1). Such improvement can be attributed to the increased absorption of $MAPbBr_3/MoS_2$ heterostructures compared to the pure MoS_2 (Fig. 3a), the effective energy transfer from $MAPbBr_3$ to MoS_2 (Fig. 3d), and a possibly higher carrier mobility within $MAPbBr_3$ NCs compared to MoS_2 [59,60]. In addition, a device based on $MAPbBr_3$ NCs showed an extremely low photoresponsivity of $\sim 7\times10^{-8}$ mA W^{-1} (Fig. S11). This could be attributed to their poor film-forming ability when deposited on a piece of paper (Fig. S12), which is in sharp contrast to the crack-free film formed by $MAPbBr_3/MoS_2$ heterostructures (Fig. S10). Based on the aforementioned TRPL analysis in Fig. 3d, it can be expected that under laser illumination, charge carriers and/or excitons were generated in the $MAPbBr_3$ NCs and readily transferred to the nearby MoS_2 nanosheets, leading to the shortened PL lifetime of $MAPbBr_3/MoS_2$ compared to $MAPbBr_3$ alone. The charge carriers and excitons were then separated in MoS_2 under the applied electric field, which finally contributed to the photocurrent. The presence of $MAPbBr_3$ NCs, despite of their poor film-forming ability, therefore compensated the poor light adsorption and photo-conversion ability of MoS_2 nanosheets with a high metallic phase concentration. Evidently, the photoresponsivity of the $MAPbBr_3/MoS_2$ device (5.6 mA W^{-1}) doubled compared to that of MoS_2 (2.76 mA W^{-1}) and increased for at least 10^7 times compared with $MAPbBr_3$ NCs ($\sim 7\times10^{-8}$ mA W^{-1}) alone. Moreover, we further compared performances of $MAPbBr_3/MoS_2$ epitaxial heterostructures with physically mixed $MAPbBr_3/MoS_2$ composite by depositing them on paper as photodetectors, and found that the *in-situ* prepared heterostructures exhibited higher photoresponsivity and on/off ratio compared with the physically mixed counterpart (Fig. 4, Fig. S13, and Table S1). Above observations further indicate the importance of using MoS_2 nanosheets as flexible substrates that connected dispersed perovskite NCs, and also enabled the effective charge and/or exciton transport through the epitaxial interfaces. The stability of the $MAPbBr_3/MoS_2$-based device was also investigated (Fig. S14), which exhibited stable current density for 2,000 s under temporal illumination by a 405 nm laser with a power of 9.6 mW, suggesting that degradation of the perovskite or phase transition in MoS_2 did not happen during the test. This is also confirmed by comparing the XRD patterns of the $MAPbBr_3/MoS_2$ hererostructures before and after 30 min of 405 nm laser irradiation, and no additional peaks due to degradation were observed (Fig. S15).

The electronic property of MoS_2 is highly dependent on its crystal structure. While 2H-phased MoS_2 is semiconducting, 1T-phased counterpart is metal-like [46]. The Li-intercalated and exfoliated MoS_2 nanosheets contain ~84% of 1T phase (Fig. S6 in SI), indicating a highly metallic nature. As a result, photodetector based on the metallic MoS_2 nanosheets hybridized with $MAPbBr_3$ NCs showed a relatively high dark current density, leading to a relatively low on/off ratio of 1.4. It has been reported previously that metallic 1T MoS_2 can be reverted back to the semiconducting 2H phase by annealing [46] or laser irradiation [61]. We therefore partially converted the MoS_2 from 1T to 2H in the $MAPbBr_3/MoS_2$ device by simply illuminating it with a 780 nm laser at 100 mW for 30 s, and the 2H concentration increased from 16% to 68% (Fig. S16), during which the $MAPbBr_3$ NCs remained stable (Fig. S17). As expected, due to the increased channel resistance after metal-to-semiconductor transition, both dark current and photocurrent considerably decreased, leading to a decreased responsivity of 0.224 mA W^{-1} (Fig. 4i). Meanwhile, the on/off ratio of the $MAPbBr_3/MoS_2$ device after laser illumination was evidently increased from 1.41 to 2.30 (Fig. 4h). Importantly, after 1T-to-2H conversion, the response times were much shortened (0.65 and 0.52 s) (Fig. 4j), which could result from the reduced defect density in MoS_2 after its transition to a more thermodynamically stable structure [37].

CONCLUSIONS

In summary, $MAPbBr_3$ NCs were directly deposited on MoS_2 in a mixed DMF/toluene solution. An optimal concentration of DMF in toluene enabled the dispersion of MoS_2 nanosheets and meanwhile ensured the precipitation of $MAPbBr_3$ NCs. The *in-situ* deposited (001)-oriented $MAPbBr_3$ NCs showed epitaxial relationship with (001) MoS_2 nanosheets by aligning along either the $MAPbBr_3$ [100]/MoS_2 [100] direction or the $MAPbBr_3$ [110]/MoS_2 [210] direction. The dispersible $MAPbBr_3$/MoS_2 epitaxial heterostructures can be directly drop-casted between two graphite electrodes drawn by pencil on a piece of paper to form a photodetector with simple configuration, and demonstrated the much improved performance compared to using MoS_2 or $MAPbBr_3$ alone due to the improved light adsorption and enhanced energy transfer. Our work suggests that despite the stringent solvation conditions, organic-inorganic hybrid perovskites could be hybridized with other functional nanostructures *via* solution-phase epitaxy. 2D materials provide flexible substrates for the epitaxial deposition of crystals even with large mismatch in lattice symmetry and parameters. Thus-obtained solution-processible heterostructures are promising for thin-film optoelectronics.

Received 4 April 2018; accepted 8 April 2018; published online 11 May 2018

1 Chhowalla M, Shin HS, Eda G, *et al.* The chemistry of two-dimensional layered transition metal dichalcogenide nanosheets. Nat Chem, 2013, 5: 263–275
2 Huang X, Zeng Z, Zhang H. Metal dichalcogenide nanosheets: preparation, properties and applications. Chem Soc Rev, 2013, 42: 1934–1946
3 Geim AK, Novoselov KS. The rise of graphene. Nat Mater, 2007, 6: 183–191
4 Karunadasa HI, Montalvo E, Sun Y, *et al.* A molecular MoS_2 edge site mimic for catalytic hydrogen generation. Science, 2012, 335: 698–702
5 Yu WJ, Li Z, Zhou H, *et al.* Vertically stacked multi-heterostructures of layered materials for logic transistors and complementary inverters. Nat Mater, 2013, 12: 246–252
6 Yu WJ, Liu Y, Zhou H, *et al.* Highly efficient gate-tunable photocurrent generation in vertical heterostructures of layered materials. Nat Nanotechnol, 2013, 8: 952–958
7 Amani M, Lien DH, Kiriya D, *et al.* Near-unity photoluminescence quantum yield in MoS_2. Science, 2015, 350: 1065–1068
8 Eda G, Maier SA. Two-dimensional crystals: managing light for optoelectronics. ACS Nano, 2013, 7: 5660–5665
9 Zhang W, Chuu CP, Huang JK, *et al.* Ultrahigh-gain photodetectors based on atomically thin graphene-MoS_2 heterostructures. Sci Rep, 2014, 4: 3826
10 Tan H, Xu W, Sheng Y, *et al.* Lateral graphene-contacted vertically stacked WS_2/MoS_2 hybrid photodetectors with large gain. Adv Mater, 2017, 29: 1702917
11 Lin J, Li H, Zhang H, *et al.* Plasmonic enhancement of photocurrent in MoS_2 field-effect-transistor. Appl Phys Lett, 2013, 102: 203109
12 Yu SH, Lee Y, Jang SK, *et al.* Dye-sensitized MoS_2 photodetector with enhanced spectral photoresponse. ACS Nano, 2014, 8: 8285–8291
13 Esmaeili-Rad MR, Salahuddin S. High performance molybdenum disulfide amorphous silicon heterojunction photodetector. Sci Rep, 2013, 3: 2345
14 Jariwala D, Sangwan VK, Wu CC, *et al.* Gate-tunable carbon nanotube-MoS_2 heterojunction p-n diode. Proc Natl Acad Sci USA, 2013, 110: 18076–18080
15 Noel NK, Stranks SD, Abate A, *et al.* Lead-free organic–inorganic tin halide perovskites for photovoltaic applications. Energy Environ Sci, 2014, 7: 3061–3068
16 Jeon T, Kim SJ, Yoon J, *et al.* Hybrid perovskites: effective crystal growth for optoelectronic applications. Adv Energy Mater, 2017, 7: 1602596
17 Sum TC, Mathews N. Advancements in perovskite solar cells: photophysics behind the photovoltaics. Energy Environ Sci, 2014, 7: 2518–2534
18 Yang WS, Noh JH, Jeon NJ, *et al.* High-performance photovoltaic perovskite layers fabricated through intramolecular exchange. Science, 2015, 348: 1234–1237
19 Chiang CH, Nazeeruddin MK, Grätzel M, *et al.* The synergistic effect of H_2O and DMF towards stable and 20% efficiency inverted perovskite solar cells. Energy Environ Sci, 2017, 10: 808–817
20 Saliba M, Matsui T, Domanski K, *et al.* Incorporation of rubidium cations into perovskite solar cells improves photovoltaic performance. Science, 2016, 354: 206–209
21 Xing G, Mathews N, Sun S, *et al.* Long-range balanced electron- and hole-transport lengths in organic-inorganic $CH_3NH_3PbI_3$. Science, 2013, 342: 344–347
22 Stranks SD, Eperon GE, Grancini G, *et al.* Electron-hole diffusion lengths exceeding 1 micrometer in an organometal trihalide perovskite absorber. Science, 2013, 342: 341–344
23 Green MA, Ho-Baillie A, Snaith HJ. The emergence of perovskite solar cells. Nat Photonics, 2014, 8: 506–514
24 Schmidt LC, Pertegás A, González-Carrero S, *et al.* Nontemplate synthesis of $CH_3NH_3PbBr_3$ perovskite nanoparticles. J Am Chem Soc, 2014, 136: 850–853
25 Pathak S, Sakai N, Wisnivesky Rocca Rivarola F, *et al.* Perovskite crystals for tunable white light emission. Chem Mater, 2015, 27: 8066–8075
26 Gonzalez-Carrero S, Galian RE, Pérez-Prieto J. Maximizing the emissive properties of $CH_3NH_3PbBr_3$ perovskite nanoparticles. J Mater Chem A, 2015, 3: 9187–9193
27 Huang H, Zhao F, Liu L, *et al.* Emulsion synthesis of size-tunable $CH_3NH_3PbBr_3$ quantum dots: an alternative route toward efficient light-emitting diodes. ACS Appl Mater Interfaces, 2015, 7: 28128–28133
28 Zhu F, Men L, Guo Y, *et al.* Shape evolution and single particle luminescence of organometal halide perovskite nanocrystals. ACS Nano, 2015, 9: 2948–2959
29 Jang DM, Kim DH, Park K, *et al.* Ultrasound synthesis of lead halide perovskite nanocrystals. J Mater Chem C, 2016, 4: 10625–10629
30 Xing J, Yan F, Zhao Y, *et al.* High-efficiency light-emitting diodes of organometal halide perovskite amorphous nanoparticles. ACS Nano, 2016, 10: 6623–6630

31 Im JH, Lee CR, Lee JW, *et al.* 6.5% Efficient perovskite quantum-dot-sensitized solar cell. Nanoscale, 2011, 3: 4088–4093
32 Niu L, Liu X, Cong C, *et al.* Controlled synthesis of organic/inorganic van der Waals solid for tunable light-matter interactions. Adv Mater, 2015, 27: 7800–7808
33 Cheng HC, Wang G, Li D, *et al.* van der Waals heterojunction devices based on organohalide perovskites and two-dimensional materials. Nano Lett, 2015, 16: 367–373
34 Lu J, Carvalho A, Liu H, *et al.* Hybrid bilayer WSe_2-$CH_3NH_3PbI_3$ organolead halide perovskite as a high-performance photodetector. Angew Chem Int Ed, 2016, 55: 11945–11949
35 Ma C, Shi Y, Hu W, *et al.* Heterostructured WS_2/$CH_3NH_3PbI_3$ photoconductors with suppressed dark current and enhanced photodetectivity. Adv Mater, 2016, 28: 3683–3689
36 Kang DH, Pae SR, Shim J, *et al.* An ultrahigh-performance photodetector based on a perovskite-transition-metal-dichalcogenide hybrid structure. Adv Mater, 2016, 28: 7799–7806
37 Wang Y, Fullon R, Acerce M, *et al.* Solution-processed MoS_2/organolead trihalide perovskite photodetectors. Adv Mater, 2017, 29: 1603995
38 Zhang F, Zhong H, Chen C, *et al.* Brightly luminescent and color-tunable colloidal $CH_3NH_3PbX_3$ (X = Br, I, Cl) quantum dots: potential alternatives for display technology. ACS Nano, 2015, 9: 4533–4542
39 Zhang F, Huang S, Wang P, *et al.* Colloidal synthesis of air-stable $CH_3NH_3PbI_3$ quantum dots by gaining chemical insight into the solvent effects. Chem Mater, 2017, 29: 3793–3799
40 Zeng Z, Yin Z, Huang X, *et al.* Single-layer semiconducting nanosheets: high-yield preparation and device fabrication. Angew Chem Int Ed, 2011, 50: 11093–11097
41 Li H, Wu J, Yin Z, *et al.* Preparation and applications of mechanically exfoliated single-layer and multilayer MoS_2 and WSe_2 nanosheets. Acc Chem Res, 2014, 47: 1067–1075
42 Heising J, Kanatzidis MG. Exfoliated and restacked MoS_2 and WS_2: ionic or neutral species? Encapsulation and ordering of hard Electropositive cations. J Am Chem Soc, 1999, 121: 11720–11732
43 Peng W, Wang L, Murali B, *et al.* Solution-grown monocrystalline hybrid perovskite films for hole-transporter-free solar cells. Adv Mater, 2016, 28: 3383–3390
44 Brunetti B, Cavallo C, Ciccioli A, *et al.* On the thermal and thermodynamic (in)stability of methylammonium lead halide perovskites. Sci Rep, 2016, 6: 31896
45 Kappera R, Voiry D, Yalcin SE, *et al.* Phase-engineered low-resistance contacts for ultrathin MoS_2 transistors. Nat Mater, 2014, 13: 1128–1134
46 Eda G, Yamaguchi H, Voiry D, *et al.* Photoluminescence from chemically exfoliated MoS_2. Nano Lett, 2011, 11: 5111–5116
47 Voiry D, Salehi M, Silva R, *et al.* Conducting MoS_2 nanosheets as catalysts for hydrogen evolution reaction. Nano Lett, 2013, 13: 6222–6227
48 Narayan J, Larson BC. Domain epitaxy: A unified paradigm for thin film growth. J Appl Phys, 2003, 93: 278–285
49 Huang X, Zeng Z, Bao S, *et al.* Solution-phase epitaxial growth of noble metal nanostructures on dispersible single-layer molybdenum disulfide nanosheets. Nat Commun, 2013, 4: 1444
50 Lin Z, Yin A, Mao J, *et al.* Scalable solution-phase epitaxial growth of symmetry-mismatched heterostructures on two-dimensional crystal soft template. Sci Adv, 2016, 2: e1600993
51 Jin M, Zhang H, Wang J, *et al.* Copper can still be epitaxially deposited on palladium nanocrystals to generate core–shell nanocubes despite their large lattice mismatch. ACS Nano, 2012, 6: 2566–2573
52 Fan FR, Liu DY, Wu YF, *et al.* Epitaxial growth of heterogeneous metal nanocrystals: from gold nano-octahedra to palladium and silver nanocubes. J Am Chem Soc, 2008, 130: 6949–6951
53 Geim AK, Grigorieva IV. van der Waals heterostructures. Nature, 2013, 499: 419–425
54 Schulz P, Edri E, Kirmayer S, *et al.* Interface energetics in organo-metal halide perovskite-based photovoltaic cells. Energy Environ Sci, 2014, 7: 1377–1381
55 Yang D, Yang R, Zhang J, *et al.* High efficiency flexible perovskite solar cells using superior low temperature TiO_2. Energy Environ Sci, 2015, 8: 3208–3214
56 Fang H, Li J, Ding J, *et al.* An origami perovskite photodetector with spatial recognition ability. ACS Appl Mater Interfaces, 2017, 9: 10921–10928
57 Lin CH, Tsai DS, Wei TC, *et al.* Highly deformable origami paper photodetector arrays. ACS Nano, 2017, 11: 10230–10235
58 Cai C, Ma Y, Jeon J, *et al.* Epitaxial growth of large-grain NiSe films by solid-state reaction for high-responsivity photodetector arrays. Adv Mater, 2017, 29: 1606180
59 Lopez-Sanchez O, Lembke D, Kayci M, *et al.* Ultrasensitive photodetectors based on monolayer MoS_2. Nat Nanotechnol, 2013, 8: 497–501
60 Stranks SD, Snaith HJ. Metal-halide perovskites for photovoltaic and light-emitting devices. Nat Nanotechnol, 2015, 10: 391–402
61 Fan X, Xu P, Zhou D, *et al.* Fast and efficient preparation of exfoliated 2H MoS_2 nanosheets by sonication-assisted lithium intercalation and infrared laser-induced 1T to 2H phase reversion. Nano Lett, 2015, 15: 5956–5960

Acknowledgements This research was supported by the National Natural Science Foundation of China (51322202), and the Young 1000 Talents Global Recruitment Program of China. Xing G acknowledges the financial support from Macau Science and Technology Development Fund (FDCT-116/2016/A3 and FDCT-091/2017/A2), Research Grant (SRG2016-00087-FST) from the University of Macau, the Natural Science Foundation of China (91733302, 61605073 and 2015CB932200), and the Young 1000 Talents Global Recruitment Program of China.

Author contributions Huang X, Xing G, and Huang W conceived the idea. Zhang Z, Sun F designed the experiments and synthesized the hybrid nanomaterial. Dai J and Sun Q exfoliated MoS_2 nanosheets. Zhu Z, Gao K and Shi X performed TEM, XRD and AFM measurements. Wei Q conducted PL and TRPL measurements. Li H, Yan Y and Yu H designed the paper-based photodetectors. All authors contributed to the general discussion.

Conflict of interest The authors declare no conflict of interest.

Supplementary information Experimental details and supporting data are available in the online version of the paper.

Zhipeng Zhang received his bachelor degree in 2015 at Nanjing Tech University. He is now a master student in the Institute of Advanced Materials (IAM) of Nanjing Tech University. His current research interest is the synthesis and applications of perovskite nanocrystals.

Guichuan Xing obtained his BSc in 2003 at Fudan University and PhD in 2011 at National University of Singapore. He joined IAM of Nanjing Tech University as a professor in 2014. His current research interest is nonlinear optical properties and ultrafast carrier dynamics in novel optoelectronic materials and devices.

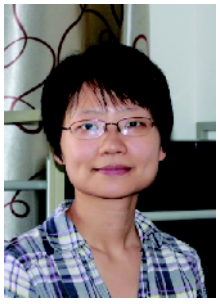

Xiao Huang received her bachelor's degree from the School of Materials Science and Engineering at Nanyang Technological University in Singapore in 2006 and completed her PhD in 2011 under the supervision of Prof. Hua Zhang and Prof. Freddy Boey. She is currently a professor at the Institute of Advanced Materials (IAM), Nanjing Tech University. Her research interest includes the synthesis and applications of two-dimensional nanomaterial-based hybrids.

Wei Huang received his BSc, MSc, and PhD degrees in Chemistry from Peking University in 1983, 1988, and 1992, respectively. He is a member of the Chinese Academy of Sciences, and a foreign member of the Russian Academy of Sciences. In 2001, he became a chair professor at Fudan University, where he founded the Institute of Advanced Materials. In June 2006, he was appointed the Deputy President of Nanjing University of Posts and Telecommunications, where he founded the Key Laboratory for Organic Electronics and Information Displays. In July 2012, he was appointed the President of Nanjing Tech University and moved to Northwestern Polytechnical University in 2017, where he is currently the Provost of Northwestern Polytechnical University. His research interest includes organic optoelectronics, nanomaterials, flexible electronics, and bioelectronics.

非传统溶液外延法在金属硫化物纳米片表面生长有机无机杂化钙钛矿纳米晶

张志鹏[1], 孙方方[1], 朱兆华[1], 戴杰[1], 高锴[1], 魏琪[1], 石晓桐[1], 孙倩[1], 闫岩[1], 李海[1], 于海东[1], 邢贵川[1,2*], 黄晓[1*], 黄维[1,3*]

摘要 基于外延异质结构的有机-无机杂化钙钛矿/二维纳米片复合材料在光电领域具有很好的应用前景, 但目前使用的固相制备方法大大限制了这一目标的实现. 我们通过精细调节溶剂环境, 成功利用外延沉积的方式实现了在三角/六方相MoS_2纳米片表面生长立方相$MAPbBr_3$($MA=CH_3NH_3^+$)钙钛矿纳米晶. 虽然$MAPbBr_3$与MoS_2存在较大的晶格不匹配度, 但是由于MoS_2纳米片性质柔软且表面缺失悬挂键, 可以在两条不同方向上观察到较高容忍度(~1%错位)的外延生长关系. 这种外延界面的形成有利于$MAPbBr_3$与MoS_2之间有效的能量转移, 因此基于$MAPbBr_3/MoS_2$异质结的纸质器件与$MAPbBr_3$或MoS_2器件相比具有更优异的光电性能. 此外, 除了提高光吸收能力和能量传递, MoS_2纳米片的存在还为离散的$MAPbBr_3$纳米晶提供柔性和连续的基底, 从而改善了$MAPbBr_3$纳米晶粒的成膜能力. 这种液相外延法可用于高性能的有机无机杂化钙钛矿与二维材料的异质结构材料的大规模制备, 将推动异质结构材料在光电领域的广泛使用.

